Dislocation plasticity in equiatomic NiCoCr alloys: Effect of short-range order

Amir H. Naghdi,[1,*] Kamran Karimi [ORCID],[1,*,†] Axel E. Poisvert [ORCID],[1] Amin Esfandiarpour [ORCID],[1] Rene Alvarez,[1]
Pawel Sobkowicz [ORCID],[1] Mikko Alava,[1,2] and Stefanos Papanikolaou [ORCID][1,‡]

[1]*NOMATEN Centre of Excellence, National Center for Nuclear Research, 05-400 Swierk/Otwock, Poland*
[2]*Aalto University, Department of Applied Physics, P. O. Box 11000, 00076 Aalto, Espoo, Finland*

Equiatomic NiCoCr solid solutions have been shown by recent experiments and atomistic simulations to display exceptional mechanical properties that have been suggested to be linked to nanostructural short-range order (SRO) features that may arise from thermal treatments, such as annealing or/and aging. Here we use hybrid Monte Carlo–molecular dynamics simulations to gain further insights of thermal effects on the SRO formation as well as the edge dislocation plasticity mechanisms of equiatomic NiCoCr face-centered cubic solid solution. For that purpose, we utilize two well-known NiCoCr interatomic potentials, one of which displays well-documented SRO, believed to be linked to experimental evidence and labeled as the Li-Sheng-Ma potential, while the other (Farkas-Caro) does not. We use these two potentials to discern short-range ordering (from inherent randomness in random solid solutions) and understand how SROs influence dislocation depinning dynamics in various thermal annealing scenarios. In this context, we used robust, scale-dependent metrics to infer a characteristic SRO size in the Li-Sheng-Ma case by probing local concentration fluctuations which otherwise indicate uncorrelated patterns in the Farkas-Caro case in a close agreement with random alloys. Our Voronoi-based analysis shows meaningful variations of local misfit properties owing to the presence of SROs. Using relevant order parameters, we also report on the drastic increase of chemical ordering within the stacking fault region. More importantly, we find that the Li-Sheng-Ma potential leads to excellent edge dislocation depinning strength with low stacking fault width. Our findings indicate an enhanced roughening mechanism due to the SROs-misfit synergy that leads to significant improvements in dislocation glide resistance. We argue that the improvements in alloy strength have their atomistic origins in the interplay between nanoscopic SROs and atomic-level misfit properties.

I. INTRODUCTION

Metallurgy of alloys is at the core of technological progress. Concentrated solid solution alloys (CSAs) have recently emerged as major candidates for novel alloys for extreme conditions applications [1,2]. Of all, the equiatomic [3] NiCoCr CSA represents a simple-enough composition that has been consistently reported to show exceptional mechanical properties [1]. These include (among others) a relatively high (tensile) strength and ductility, fracture toughness, as well as (micro-)hardness that often exceed those of the "Cantor" alloy [4] yet with a fewer number of principal components. This is most likely rooted in the chemical composition and underlying substructure. However, the microstructural origin of the exceptional mechanical properties has been heavily debated, with a possible explanation being the presence of nanometer-level (chemical/structural) short-range order (SRO) [5–8] that arises from particular thermal

processing and influences dislocation pinning and stacking fault widths. In addition, lattice distortions and local crystalline misfits, due to atomic size differences [9,10], have been shown to be correlated to the exceptional mechanical behavior of this alloy. Given the apparent importance of local misfit volumes [9], it remains a challenge to identify the role of SRO for exceptional mechanical properties. In this paper, we focus on extensive molecular simulations to understand how SRO influences dislocation plasticity and how it might depend on processing parameters (i.e., annealing temperature), the properties of the ordered phase, as well as the role of the MD atomic potentials in the ordering process. In this framework, we investigated two case studies involving commonly used NiCoCr interatomic potentials Li-Sheng-Ma (LSM) and Farkas-Caro (FC) potential. While LSM leads to the formation of short-range ordering on aging, FC displays chemical/structural features, under the exact same thermal treatment, that are almost indistinguishable from random solid solutions. Our multiscale characterization of local ordering was based on the use of novel descriptors that exhibit distinct structural/chemical signatures owing to the presence of nanoscopic SROs. We study the effects of the SRO on mechanical properties, showing that it significantly influences them via the interplay of dislocations and SRO structures. Such an interplay was quantified via a detailed analysis of the dislocation substructure indicating enhanced roughening properties due to combined SRO-misfit effects.

---

*These authors made equal contributions.

†kamran.karimi@ncbj.gov.pl

‡Stefanos.Papanikolaou@ncbj.gov.pl

Short-range order has been at the core of studies in CSAs across the board [11–13]. Thermodynamically speaking, SROs' ubiquity at low-temperature alloys has been mainly attributed to dominant enthalpic effects that, in the absence of entropy-driven mechanisms, do not favor idealistic perfect mixtures of equimolar elements [14]. In this context, SROs typically refer to coherent compositional deviations apart from (statistically) random distributions of atoms within the solution matrix as in random solid solution alloys (RSAs). More importantly, (thermal) processing parameters associated with annealing and homogenization procedures (i.e., temperature and time) or irradiation may have a drastic effect on the nucleation of SROs and associated substructural features [9,15,16]. Owing to their nanoscopic scales, laboratory-based observations of SROs are quite nontrivial involving intensive use of advanced characterization techniques such as high-resolution electron microscopy and atomic-resolution energy dispersive spectrometry mapping [8,17]. The latter are strongly tied to underlying physical mechanisms that govern fundamental alloy properties. For instance, the formation of Ni-rich nanoprecipitates and associated inhomogeneities within the annealed NiCoCr matrix has been recently suggested to tune the stacking fault width with evident consequences in terms of the alloy strengthening [14,18]. Similar conclusions were drawn experimentally by Ritchie *et al.* [5], who reported on the emergence of SROs in aged NiCoCr CSAs with significant impacts on the dislocation activation energy and hardness. In studies of NiCoCr-based alloys, stacking fault energy, hardness, and fracture toughness, as bulk properties, were recently shown to strongly correlate with the degree of Ni-rich SROs and corresponding structural features [19–22].

In contrast, local misfit properties have been conventionally viewed as a key solid solution strengthening mechanism [23]. In this framework, the inherent yield strength of alloys (or Peierls stress) associates to the stress threshold required for dislocation depinning, and in the context of multicomponent high-entropy alloys, their intrinsic hetrogeneity and randomness gives rise to somewhat uncorrelated perturbations to the local thresholds. This concept was theoretically put forward in the seminal work by Labusch [24], who hypothesized that the motion of dislocations within a random set of solute obstacles leads to significant hardening effects in dilute solutions. In a series of relevant papers, Varvenne and Curtin (VC) [25–27] further investigated the RSA context in terms of elastic-type long-range interactions between dislocation lines and residual strain fields resulting from atomic size misfits. Along these lines, a mean-field theoretical framework was proposed to make fairly accurate predictions of yield strengths solely based on the effective medium elastic properties and, more importantly, local misfit fluctuations. The proposed theory accounts for local compositional fluctuations described by spatial distributions of misfit volumes which are accessible through atomistic simulations and experimentation. The VC framework was further generalized to additionally account for thermal and strain-rate effects on the alloys' strength and checked in the context of random alloys [9,26]. In the case of high-entropy alloys (HEAs), however, there may often be a considerable degree of short-range

ordering and, therefore, HEAs cannot be simply treated as fully random.

Short-range order and local misfits are not one-way streets but they combine and interplay in ways that are somewhat unpredictable in advance and inseparable [20]. Moreover, almost all crucial properties related to alloy strengths are strongly dependent on the underlying microstructure and processing methods used to synthesize CSAs. In an aged multicomponent alloy, the effective Peierls stress will be influenced by both randomness in the local composition distribution (giving rise to misfit fluctuations) and short-ranged (but still finite) spatial correlations introduced by SROs. Naturally, this combined effect leads to an effective yield stress that typically exceeds that of a random solid solution, lacking this finite-range ordering component. A naive picture in this context is that dislocations will move by locally bending between pinning sites to overcome locally fluctuating Peierls stresses leading to extra strengthening [28]. Nevertheless, a systematic study accounting for dislocations' glide resistance and their substructure discerning the separate roles of SROs and misfits seems necessary.

To this end, we use a versatile approach to investigate the microstructural/chemical origin of strengthening in NiCoCr including enthalpy-driven ordering effects and local distortions. We perform hybrid Monte Carlo–molecular dynamics (MC-MD) simulations at a range of annealing temperatures based on two commonly used NiCoCr interatomic potentials. We find that the emergence of SROs is not a robust feature of annealed model NiCoCr CSAs but, to a great extent, depends on the chosen potential energy. More specifically, the two models generate microstructurally different alloys (with/out SROs) with the exact same thermal processing. Following the numerical framework in Ref. [14], we probed effects of SROs in terms of local concentration fluctuations, stacking fault widths, dislocation glide resistance, and misfit volumes of NiCoCr as well as thermodynamic properties such as the specific heat and thermal expansion coefficient. Our analysis indicates meaningful correlations of the above observables with varying degrees of SROs in aged alloys, making them easily distinguishable from RSAs. We further observe a marked growth in the population of SROs inside the stacking fault region and remarkable strengthening behavior against dislocation glide with the latter rooted in the interplay between short-range ordering and local misfit properties.

The organization of this paper is the following. In Sec. II, we describe the numerical setup, sample preparation (including aging/annealing), loading protocols, and relevant simulation details including the hybrid MC-MD model, interatomic forces, and shear test description. Section III presents our simulation results relevant to the chemical/microstructural characterization of SROs and their potential effects on dynamics of dislocations. In this context, Sec. III A introduces robust structural/compositional metrics associated with local elemental fluctuations to characterize the temperature dependence of SROs and distribution of misfit volumes. Lattice distortions in the presence of short-range ordering will be discussed in Sec. III B. In Sec. III C, we provide an in-depth analysis of partial dislocations and their depinning mechanism in the presence of SROs. This includes autocorrelation

analyses associated with the dislocation line fluctuations as well as local variations of the dislocation velocity. Section IV presents relevant discussions and conclusions.

II. METHODS AND MATERIALS

Molecular dynamics simulations were carried out in LAMMPS [29] by implementing atomistic samples of size $N = 500\,000$ and $1\,700\,000$ within a three-dimensional periodic cell. In order to study SRO properties (in the absence of dislocations), we prepared cubic samples with length 10 nm along the $x[100]$, $y[010]$, and $z[001]$ directions. The NPT ensembles were implemented via a Nose-Hoover thermostat and barostat with relaxation timescales $\tau_d^{\mathrm{therm}} = 10$ fs and $\tau_d^{\mathrm{bar}} = 100$ fs. We also set the discretization time to $\Delta t \simeq 1.0$ fs. Samples were initially prepared via an energy minimization at $T = 0$ K (at a fixed volume) and subsequently thermalized at different temperatures and constant pressure $P = 0$ bar for 100 ps prior to annealing.

The interatomic forces are based on two commonly used embedded-atom method (EAM) potentials in the context of NiCoCr solid solution alloys: (i) the Li-Sheng-Ma potential proposed in Ref. [14], which has been utilized in recent SRO studies, modeling dislocation nucleation and glide dynamics [20,30], and nanoindentation tests [19] and (ii) the EAM Farkas–Caro potential [31], originally developed to model equimolar high-entropy FeNiCoCrCu alloys but used here to validate the SRO formation and its robustness against different potentials.

Annealed configurations were obtained performing hybrid MC-MD simulations based on the variance constrained semi-grand-canonical (VCSGC) ensemble [32] within the annealing temperature range $T_a = 400$–1300 K. To determine the values of $\Delta\mu_{X_1 X_2} = \mu_{X_1} - \mu_{X_2}$ minimizing the composition errors, we perform a set of semi-grand-canonical simulations by varying the chemical composition at $T = 1500$ K and fit the MC data based on the equation: $\Delta\mu(X_1, P, T) = T\ln(X_1/[1 - X_1]) + \sum_{i=0}^{n} A_i X_1^i$ (see Fig. S1 in the Supplemental Material [33]). Here X_1 is the reference element (Ni in our work) and A_i's are the fitting parameters [34]. This allows us to perform hybrid MD/VCSGC-MC with a fixed target composition. During the annealing process, we perform 1 MC cycle consisting of $N/2$ attempts of transmutation every 20 MD steps. We carried out a total number of $800\,000$ MC cycles at all annealing temperatures T_a to ensure that the configurations reach thermal equilibrium and that the structure of SROs are statistically indifferent.

We also studied dynamics of a $\frac{1}{2}[\bar{1}10](111)$ edge dislocation which, under an external perturbation, dissociates into two separate partials with a stacking fault in face-centered cubic (fcc) crystals. To this end, we constructed a simulation cell with dimensions $L_x \simeq 80$, $L_y \simeq 20$, and $L_z \simeq 15$ nm (see Fig. S2) and performed annealing at a desired temperature T_a. We subsequently equilibrated the annealed alloy at a low temperature $T = 5$ K and pressure $P = 0$ for the duration of 100 ps. To create an edge dislocation within the aged sample, we used the periodic array of dislocation model proposed in Ref. [35] to ensure a periodic setup along the Burgers vector ($x[\bar{1}10]$) and dislocation line ($z[\bar{1}\bar{1}2]$). The dislocated sample was further relaxed using the NPT framework

with $P_{xx} = P_{zz} = 0$ and $T = 5$ K (for 100 ps) leading to the dislocation dissociation into two Shockley partials. Shear tests were performed at $T = 5$ K in order to suppress thermal activation and isolate sole effects of local lattice distortion and SROs on yield properties. To this end, a stress-controlled framework was employed within the NVT ensemble by applying additional forces on the top plane (normal to y) with the bottom layer held fixed (with a thickness $\simeq 4$ Å) during the course of shear simulations. The applied stress was gradually increased from $\sigma = 50$ MPa (in a quasistatic fashion) above a critical (depinning) stress in order to move the partial dislocations.

III. RESULTS

The above methodology to prepare and anneal model CSAs indicates that aged NiCoCr alloys may exhibit varying degrees of chemical ordering under different annealing temperatures. Using robust composition-based metrics in Sec. III A, we further confirm the formation of SROs and their strong dependence on the thermal processing. Section III B presents the misfit volume analysis indicating meaningful correlations with the degree of short-range ordering. In Sec. III C, we analyze dynamics of partial dislocations in the presence of SROs and discuss potential implications in terms of the SRO-induced CSA strengthening.

A. Temperature dependence of SROs

Figure 1 illustrates that the formation of SROs within the solid solutions may strongly depend on the annealing temperature T_a. The color map of atoms, the inset of Fig. 1(a), indicates a clear segregation of Ni-rich phases (gray circles) in the NiCoCr CSA modeled via the Li-Sheng-Ma potential at $T_a = 800$ K. Overall, the observed clustering features tend to become less pronounced at higher annealing temperatures as shown in Fig. S3.

The presence of SROs appears to have a direct relevance on the (constant-pressure) heat capacity $C_p = \partial_T H$ in Fig. 1(a) featuring a maximum around $T_a \simeq 800$ K. Here H denotes the enthalpy [36]. The data presented in Fig. 1 correspond to a sample equilibrated at $T = 300$ K and subsequently aged at multiple annealing temperatures. The emerging peak in C_p may suggest a dominant role of enthalpic interactions over entropic effects that rule out the formation of an ideal random solid solution [14]. We note that the (ideal) heat capacity associated with the latter rises monotonically within the temperature range of interest. Such deviations seem to be less pronounced in terms of the thermal expansion coefficient $\alpha_p = \frac{1}{V}\partial_T V$, with V being the system volume, as shown in Fig. 1(b).

The notion of SROs typically refers to coherent compositional deviations from (statistically) random distributions of atoms within the solution matrix. Along these lines, we investigated the Warren–Cowley SRO parameters $p_{ab}(r)$ [13] probing the concentration variations of type-b atoms at a distance r from a center type-a element. For an equimolar random NiCoCr solid solution, one obtains $p_{ab}^{\mathrm{rsa}} = 0.33$ (on average) at any r—more precisely, between the successive valleys of the pair correlation function $g(r)$ as in Fig. 2(g). The SRO parameters could be also determined locally for
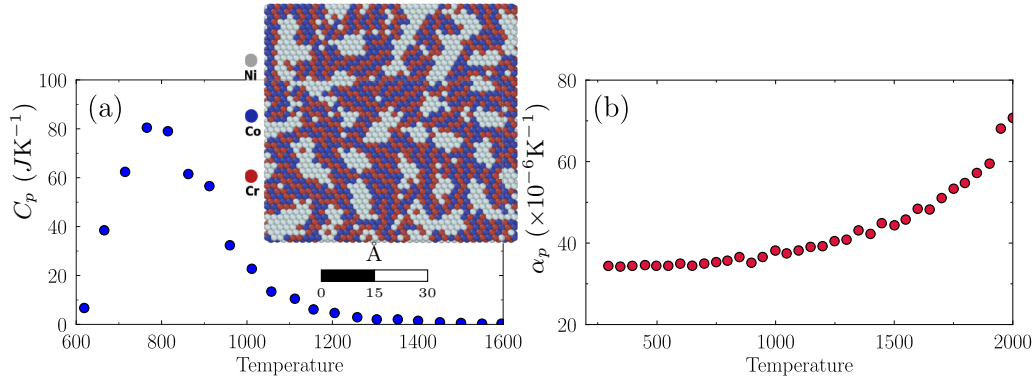
FIG. 1. Annealing temperature effects on NiCoCr based on the Li-Sheng-Ma potential. (a) Heat capacity C_p and (b) thermal expansion coefficient α_p versus anealing temperature T_a. The inset represents a (111) cross section of Ni (gray), Co (blue), and Cr (red) atoms at $T_a = 800$ K.

individual atoms which will presumably show strong fluctuations in the presence of SROs. Nevertheless, the "averaged" Warren–Cowley parameters should be relevant as the system tends to be statistically homogeneous beyond the mean SRO size.

Figures 2(a)–2(f) illustrates deviations of p_{ab} associated with the annealed CSAs from p_{ab}^{rsa} including the six (distinct) elemental pairs at $T_a = 400$ K. The order parameters reveal several interesting features describing the SRO microstructure. The abundance of the Ni-Ni pairs beyond random concentrations is remarkable and appears to persist up to $r \simeq 5$ Å in Fig. 2(a). It should be noted that twice this lengthscale is in a rough agreement with the visual impression one gets from the segregation map, the inset of Fig. 1(a), regarding the mean SRO size. Below the base line, the dip in p_{ab}

corresponding to Ni-Ni pairs should indicate their scarcity above the mean size. The order parameter recrosses the horizontal line beyond which it features a fairly broad peak at $r \simeq 15$ Å before going asymptotically to p_{ab}^{rsa}. We remark that the inferred lengthscale could potentially relate to the average spacing between adjacent SROs. Figures 2(b) and 2(c) associated with p_{NiCo} and p_{NiCr} feature fairly identical properties but with opposite trends as seen in p_{NiNi} since they must all add up to unity.

As opposed to Ni-Ni ordering, we observe fewer coherent patterns associated with the identical (same-element) pairs Co-Co and Cr-Cr as in Figs. 2(d) and 2(f). In particular, p_{CoCo} and p_{CrCr} seem to indicate ordering as well as antiordering (potentially due to repulsion) at the first- and next-nearest-neighbor distances. The strong bonding between Co-Cr in
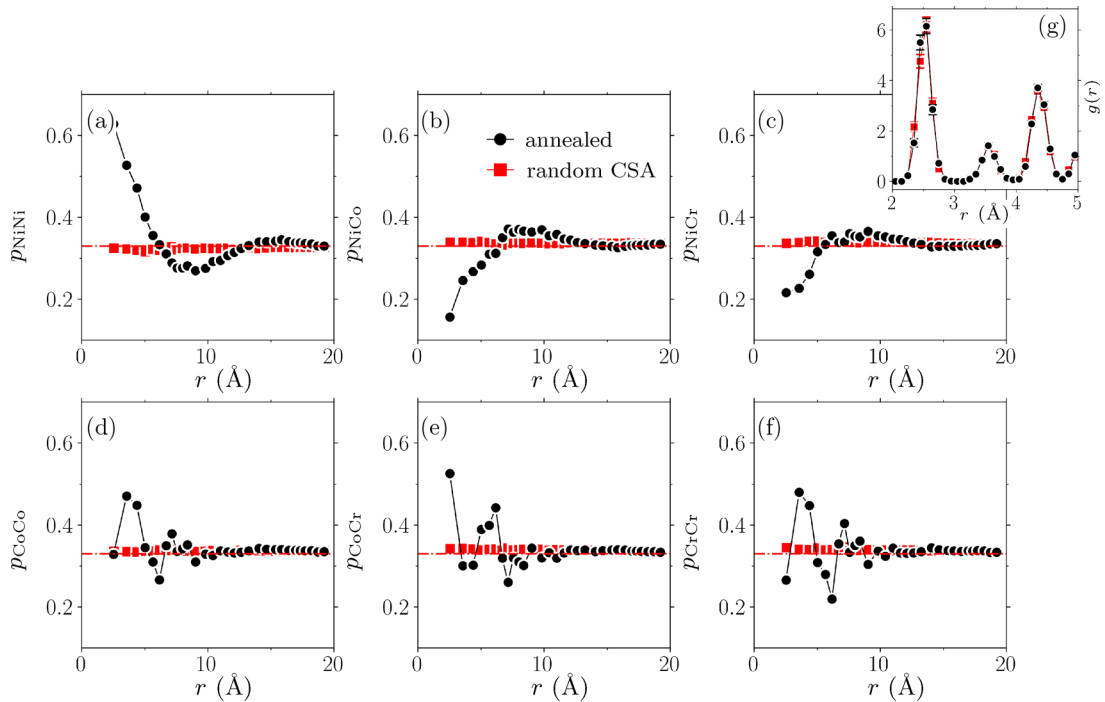

FIG. 2. Short-range ordering in annealed NiCoCr CSAs based on the Li-Sheng-Ma potential. Warren–Cowley SRO parameters including (a) p_{NiNi}, (b) p_{NiCo}, (c) p_{NiCr}, (d) p_{CoCo}, (e) p_{CoCr}, and (f) p_{CrCr} plotted against distance r at $T_a = 400$ K. (g) Pair correlation function $g(r)$ at $T_a = 400$ K. The base (red) dash-dotted line indicates the random concentration.
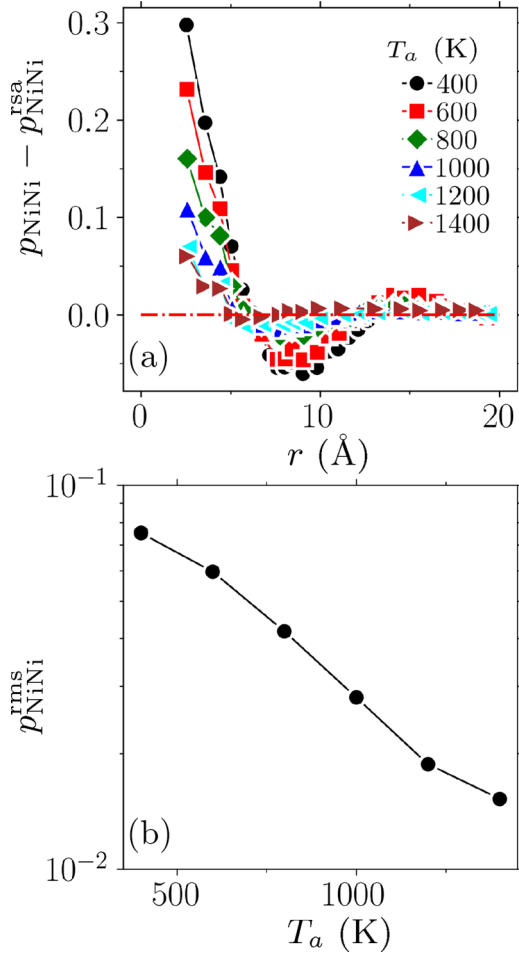
FIG. 3. SRO variations with annealing temperature T_a. (a) p_{NiNi}-p_{NiNi}^{rss} as a function of pair distance r and (b) root-mean-squared fluctuations p_{NiNi}^{rms} plotted against T_a. The (red) base line indicates zero correlations associated with RSAs. The results are based on the Li-Sheng-Ma interatomic potential.

FIG. 4. Root-mean-squared (rms) fluctuations p_b^{rms} of local Ni, Co, and Cr concentrations as a function of window size r_c in (a) annealed NiCoCr CSAs at $T_a = 400$ K and (b) NiCoCr RSAs at $T = 400$ K based on the Li-Sheng-Ma potential. The panels in (c) and (d) are the same as in (a) and (b) but with the y axis rescaled by $r_c^{-\frac{3}{2}}$. The curves are shifted for the sake of clarity.

Fig. 2(e) at the first nearest neighbor is also remarkable (see also Refs. [14,19,20]). We further note that, unlike p_{ab}, the pair correlation function $g(r)$ does not suggest any *structural* differences between annealed and random solid solutions as shown in Fig. 2(g).

Figure 3 quantifies the abundance of Ni-Ni elemental pairs on annealing at multiple temperatures between $T_a = 400$–1400 K. As shown in Fig. 3(a), the curves show quite complex nonmonotonic features with certain characteristic lengthscales that seem to scale nontrivially with temperature. Nevertheless, the SRO-related features in p_{NiNi}-p_{NiNi}^{rsa} become less and less pronounced with an increase in T_a continually approaching their asymptote at the zero-valued base line. This is mathematically quantified by the metric $p_{NiNi}^{rms} = \langle (p_{NiNi} - p_{NiNi}^{rsa})^2 \rangle^{\frac{1}{2}}$ as a root-mean-squared (rms) measure of deviations from RSAs. Figure 3(b) features a monotonic growth of p_{NiNi}^{rms} on decreasing T_a. We also note the tendency for the saturation of p_{NiNi}^{rms} at $T_a \simeq 1400$ K or above potentially due to residual SRO distributions at atomistic levels that preclude an ideal RSA formation. The above analysis was repeated for NiCoCr alloys simulated based on the Farkas-Caro potential. Inter-
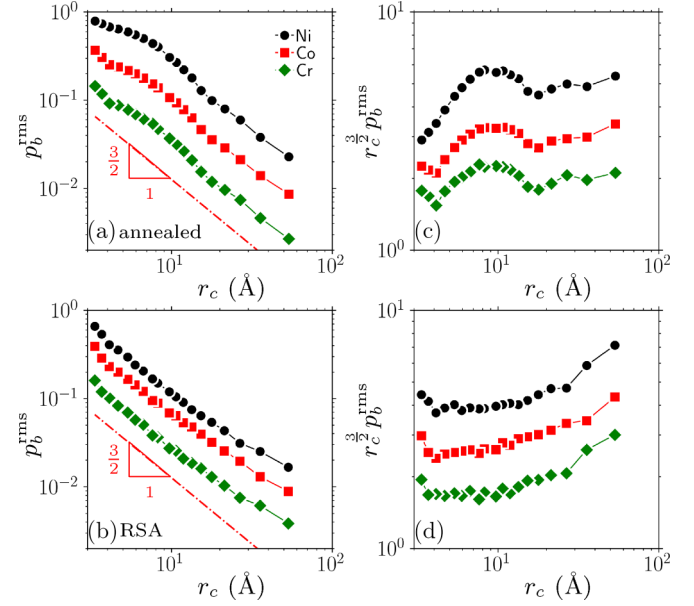
estingly, we found no clear signature of clustering in these samples as opposed to those generated via the Li-Sheng-Ma potential (see Fig. S4).

We probed fluctuations in *local* concentrations of the constituent elements in annealed NiCoCr alloys that, in the presence of SROs, should deviate from those of random solid solution alloys. In this context, the entire space was partitioned using subvolumes of varying size r_c, and local molar compositions p_{Ni}, p_{Co}, and p_{Cr} were determined within each cube. As illustrated in the scatter plot of Fig. S5 associated with NiCoCr CSAs annealed at $T_a = 400$ K, the fluctuations tend to self-average at larger r_c which could be also understood in terms of counting statistics.

We also investigated *local* fluctuations in CSA elemental concentrations in space that, in the presence of SROs, show marked deviations from those of RSAs. Figure 4 shows rms fluctuations of local concentrations p_{Ni}, p_{Co}, and p_{Cr} and their decay with distance r_c. In Figs. 4(a) and 4(c), rms fluctuations in annealed NiCoCr CSAs seem to self-average but only above some certain lengthscale above which the decay is well predicted by the expected $r_c^{-3/2}$ power-law behavior. The latter is the relevant scaling in purely random atomic configurations as illustrated in Figs. 4(b) and 4(d). We take the characteristic peak in Fig. 4(c) as a signature of spatial correlations which may be interpreted as the average SRO size $\xi^{sro} \simeq 10$ Å. Furthermore, the inferred lengthscale closely agrees with the one extracted from the SRO order parameters in the preceding paragraphs which is within the typical range of SRO size (0.5–1.5 nm) seen experimentally [5,17]. Figure 5 illustrates the probability distribution functions (PDFs) of the local Ni concentrations p_{Ni} at $r_c = 10$ Å for different annealing temperatures. We note the marked deviation of the
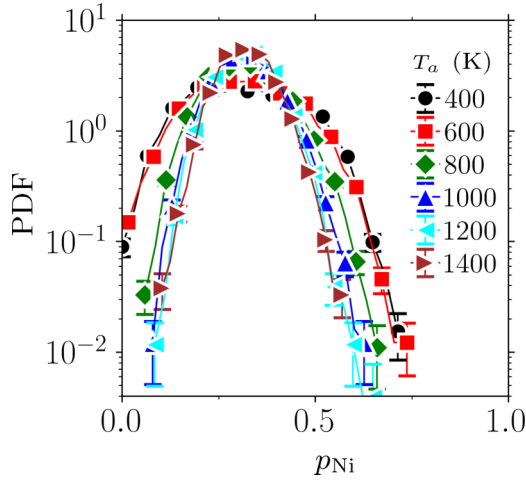
FIG. 5. Probability distribution functions of the local concentrations p_{Ni} in an annealed CSA based on the Li-Sheng-Ma potential at the window size $r_c = 10$ Å and various T_a.

low-T_a PDFs from a standard Gaussian distribution which, otherwise, seems to be the asymptotic limit for the p_{Ni} distributions at higher annealing temperatures. One could also observe a marked abundance of low and high (local) Ni concentrations away from the average at $p_{Ni} = 0.33$ for $T_a = 400$ and 600 K which is indicative of the strong segregation of Ni phases.

B. Lattice distortions

To characterize local distortion properties, we analyzed fluctuations in atomic Voronoi cell volumes and associated temperature dependence in annealed alloys. The aged solid solutions were equilibrated at 5 K on annealing in order to suppress thermal fluctuations. Figures 6(a) and 6(b) shows alloy atomic volumes and associated PDFs for the Ni, Co, and Cr atoms in annealed and random solid solutions. Both alloys feature quite narrow distributions with well-defined mean values $\langle V_{Ni}\rangle$, $\langle V_{Co}\rangle$, and $\langle V_{Cr}\rangle$ that show slight variations with T_a as in Fig. 7(a). The measured mean atomic volume in annealed NiCoCr samples is $\langle V\rangle \simeq 11.3$ Å^3—which is equivalent to the average lattice constant of $a = 3.56$ Å—in very close agreement with experimental observations reported in Ref. [9]. Figure 7(a) indicates features near a characteristic annealing temperature $T_a \simeq 800$ K below which the mean atomic volumes seem to accelerate, potentially a signature of remarkable enthalpy-driven ordering [14]. This observation is in accordance with the heat capacity C_p developing a characteristic peak in Fig. 1(a).

The misfit volumes $\Delta V_b = \langle V_b\rangle - \langle V\rangle$ of Ni, Co, and Cr are determined as $+0.04$, -0.03, and -0.01 Å^3, respectively. The estimated atomic misfits appear to be at least one order of magnitude off from precise experiments [9] but are otherwise reasonably close to *ab initio*–based estimates in Ref. [37]. We further explored the scaled fluctuation $\mathrm{var}^{\frac{1}{2}}(V_b)/\langle V_b\rangle$ as a relevant measure of atomic distortions in Fig. 7(b) with b denoting Ni, Co, and Cr. $\mathrm{var}^{\frac{1}{2}}(V_b)/\langle V_b\rangle$ shows a (fairly) monotonic increase for Ni as a function of T_a until it saturates at a limiting value that appears to be lower than the one
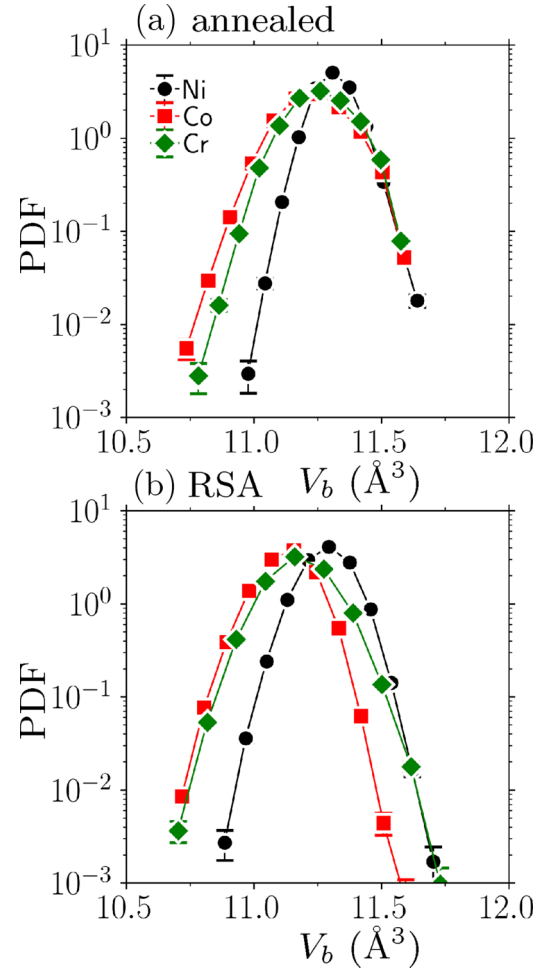

FIG. 6. Probability distributions of alloy atomic (Voronoi) volumes V_b with b denoting the Ni, Co, and Cr atoms in (a) the NiCoCr alloy aged at $T_a = 600$ K and (b) NiCoCr RSA. The volume measurements were carried out at 5 K.

set by the RSA. This is in line with our SRO analysis that the abundance of Ni-Ni pairs within the first-nearest-neighbor distance and, therefore, ordering tends to curtail local atomic misfits or randomness in aged systems. As for Co and Cr, we observe a nonmonotonic evolution with a pronounced peak at $T_a \simeq 600$ K that, in the case of the former, even exceeds the associated RSA limit. Apart from the observed peaks, the relative variance for aged Co/Cr seem to always fall short of those of RSAs with a more dramatic decrease associated with Cr (the green diamonds). This, we conjecture, might be attributed to the favored formation of Cr-Co regions and less tendency for Cr-Ni as well as Cr-Cr bonding as evidenced by the behavior of the first-nearest-neighbor order parameters in Fig. 2. We conclude this subsection by stating that short-range order will have strong bearings on misfit volumes of NiCoCr as our data suggest direct correlations between the latter and the order parameters presented in Sec. III A. One may infer a characteristic scale based on the rms fluctuations analysis presented in Fig. 7(b) which we interpret as the (mean) misfit size $\xi^{\mathrm{misfit}} \simeq 1$ Å. Together with nanoscopic SROs ($\xi^{\mathrm{sro}} \simeq 10$ Å), atomic-level misfit fluctuations will determine the dislocation glide resistance as discussed in Sec. III C.

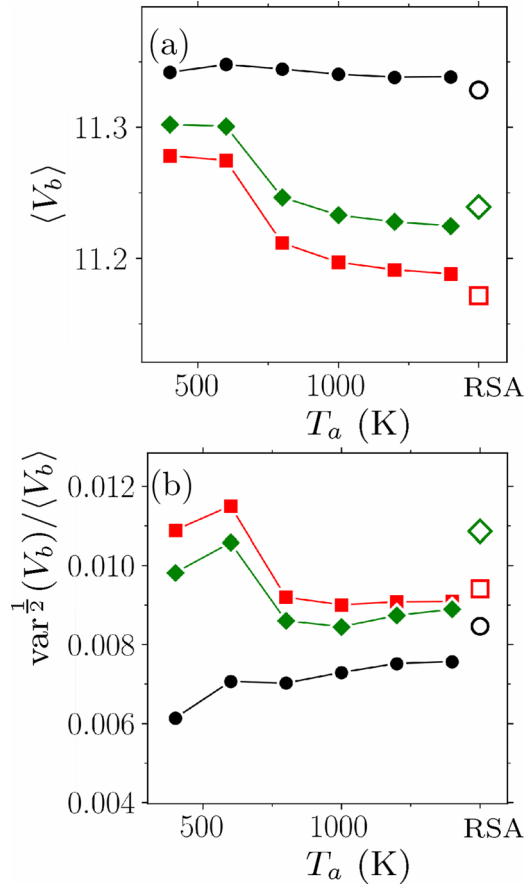FIG. 7. Dependence of (a) average Voronoi volume $\langle V_b \rangle$ and (b) rms volume fluctuations scaled by the average value $\mathrm{var}^{\frac{1}{2}}(V_b)/\langle V_b \rangle$ on the annealing temperature T_a. The empty symbols correspond to a NiCoCr RSA.

C. Interplay between SROs and dislocations

We follow two different approaches to address the dislocation-SRO interplay in NiCoCr CSAs: (i) study of dislocation effects on the nucleation of SROs in *aging* alloys and (ii) investigations of strengthening mechanisms at play in *as-aged* SRO-rich alloys driven out of equilibrium. In (i), we aged samples with a dislocation allowing for both the dislocation dissociation process and spatiotemporal evolution of SROs while annealing. In (ii), on the other hand, we embedded partial dislocations in as-annealed alloys and performed shear depining tests, with no appreciable change in the SRO microstructure.

In line with (i), Fig. 8 compares the structure of SROs within the dislocation dissociation bounds and outside in aging NiCoCr at $T_a = 600$ K. In Fig. 8(a), the denser population of SROs within the stacking fault is visually apparent in comparison with a dislocation-free two-dimensional stack at $y = 10$ Å illustrated in Fig. 8(b). We quantified the observed trend in Fig. 8(c) where the SRO parameter p_{NiNi} associated with the former reveals a shallower decay relative to that of atoms outside the fault plane. To our knowledge, the drastic increase in chemical ordering within the stacking fault region has not been previously reported in the literature. As one possible mechanism at play, we speculate that the long-range
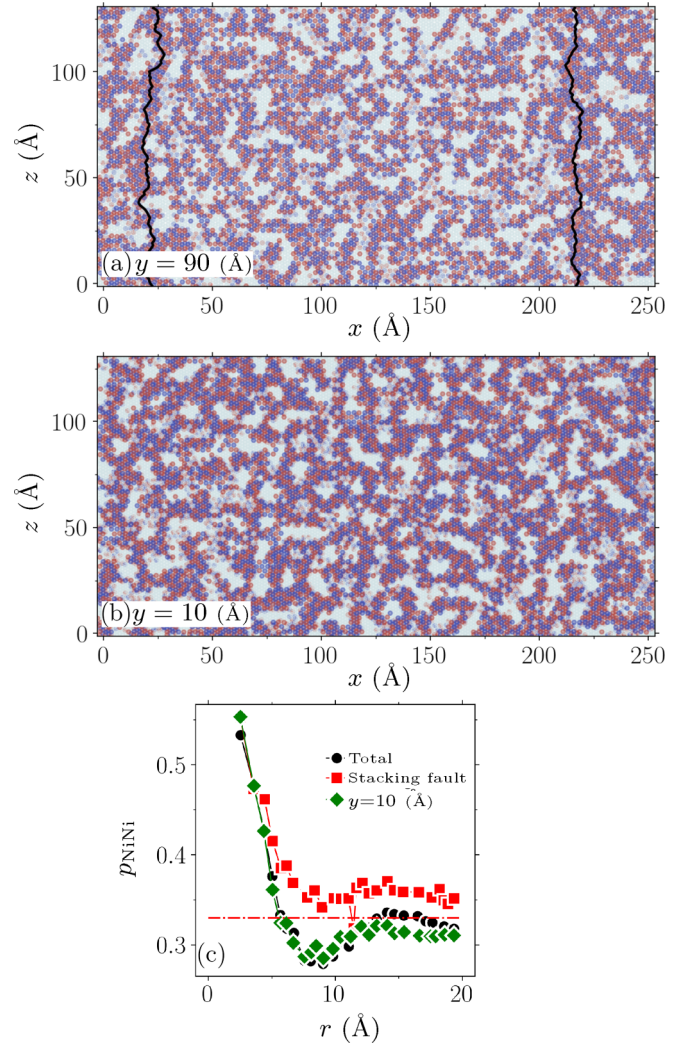

FIG. 8. SRO microstructure in the presence of (partial) dislocations in aging NiCoCr at $T_a = 600$ K. (a) Cross section containing the stacking fault, (b) cross section at $y = 10$ Å, and (c) the SRO parameter p_{NiNi} as a function of pairwise distance r. The different curves in (c) correspond to the entire configuration as well as the two-dimensional stacks depicted in (a) and (b). The black segments denote dislocation lines. The dash-dotted (red) line indicates RSAs. The stacking fault region in (a) lies between $x \simeq 25$ and 220 Å.

stress field and mutual interactions between the two partials [38] might favor the SRO nucleation and its growth within the dissociation zone. Figure S6(a) and S6(b) illustrates that such interactions at $T_a = 600$ K lead to a notable reduction in the stacking fault width which implies the enhanced fault energy due to SROs [14,18]. It is expected that the fault dimension, and therefore the associated formation energy, will be strongly controlled by the annealing temperature as well. We note that a detailed description of the SRO kinetics and dynamics of the dislocation dissociation as well as their (dynamical) interplay during the aging processs is outside the scope of our current study.

Following approach (ii), the notion of "plastic flow" in solute strengthening theories directly links to the existence of the intrinsic friction stress σ_c beyond which dislocations tend

to glide rather smoothly at a non-negligible (mean) velocity $\langle v \rangle$. Below this critical stress, by contrast, the migration of dislocations within CSAs (with a severely distorted energy landscape) typically occurs in a very intermittent manner with long periods of quiescent states (i.e., $\langle v \rangle \simeq 0$) interrupted by bursts of displacements [39]. In the absence of thermal activation, this depinning transition is phenomenologically described as [40]

$$\langle v \rangle \propto (\sigma - \sigma_c)^{1/\beta}, \qquad (1)$$

at $\sigma \geqslant \sigma_c$ and $\langle v \rangle = 0$ otherwise, with $\beta \geqslant 1$ reflecting a marked discontinuity at σ_c [41]. Here σ is the applied shear stress resolved in the glide plane.

To estimate σ_c, we performed atomistic simulations of dislocation properties in fcc-based NiCoCr CSAs by studying dynamics of $\frac{1}{2}\langle 110 \rangle \{111\}$ edge dislocations which, under an external drive, dissociate into two mixed partials and a stacking fault in between [38]. To measure the dislocation velocity and its spatial-temporal evolution, we first identified all dislocation line defects in the atomistic crystal, along with their Burgers vectors, and output a line representation of the dislocations by using OVITO [42]. Due to inherent lattice distortions, dislocation lines are not straight but show local fluctuations with respect to the average line direction along z. We describe line fluctuations projected along the glide direction x by the function $h_x(z)$ discretized via a fine grid of size 2 Å across the glide plane parallel to the z direction. We obtain the dislocation velocity $v_x(z) = \delta h_x(z)/\delta t$ by considering successive dislocation snapshots that are apart by the time window $\delta t \simeq 4$ ps. The latter is chosen to be at least three orders of magnitude longer than the discretization time Δt yet short enough to resolve displacements down to atomistic scales. The subsequent correlation analysis was performed on CSAs initially annealed at $T = 600$ K and sheared, along with the RSAs, at 5 K.

Figures S7 and S8 illustrate configurations of (frozen) dislocations in an annealed NiCoCr as well as a NiCoCr RSA under different loads well below the depinning transition ($\sigma < \sigma_c$). The local curvatures associated with the dislocation segments in Fig. S7 indicate fairly coherent pinning effects that somewhat correlate with the spatial locations of SROs. Such features might be also present in RSAs, as in Fig. S8, but to a very limited extent in space. The local line curvature, and its positive sign with respect to the glide direction, should potentially indicate how effectively dislocations are pinned near SROs and/or due to local atomic misfits. In this context, line fluctuations associated with the aged alloy in Fig. 9(a) appear to be correlated over larger lengthscales than those of the random alloy in Fig. 10(a). Similar trends could be also inferred from the associated correlation functions

$$c_h(|z - z'|) = \langle\, \hat{h}_x(z).\hat{h}_x(z') \,\rangle, \qquad (2)$$

with the z-scored fluctuations $\hat{h}_x = (h_x - \langle h_x \rangle)/\text{var}^{\frac{1}{2}}(h_x)$. Here the angular brackets $\langle . \rangle$ denote averaging in space. Overall, the slower decay of correlations $c_h(|z - z'|)$ in Fig. 9(b), in comparison with Fig. 10(b), may indicate additional SRO-induced pinning effects in annealed alloys. We note that the absence of SROs does not necessarily rule out long-
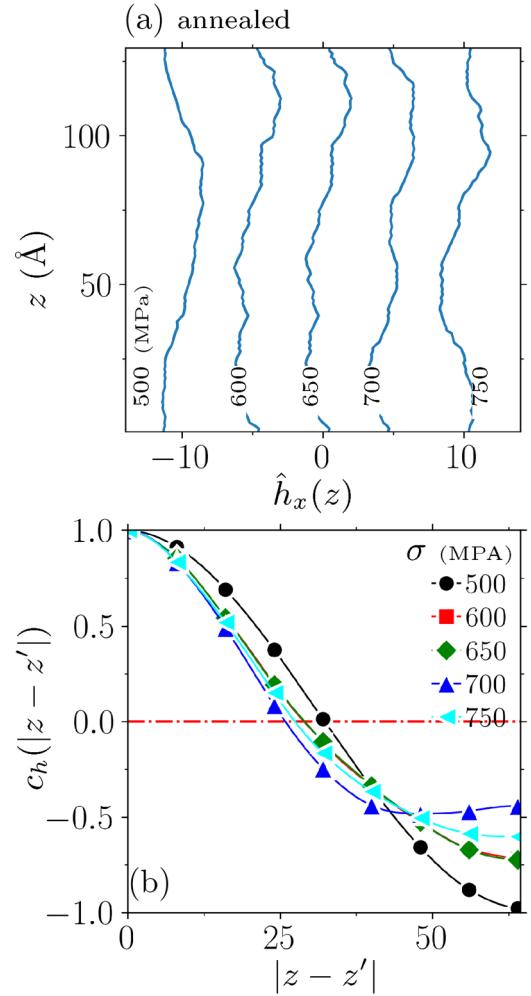

FIG. 9. (a) Configurations of (immobile) partial edge dislocations and (b) associated correlations $c_h(|z - z'|) = \langle\, \hat{h}_x(z).\hat{h}_x(z') \,\rangle$ as a function of distance $|z - z'|$ in an annealed NiCoCr under different applied stresses (below the depinning transition) at $T_a = 600$ K. This includes $\sigma = 500$, 600, 650, 700, and 750 MPa. The shear tests were carried out at 5 K. Here the two-dimensional x-z glide plane denotes a (111) cross section. The dislocation configurations are shifted vertically for the clarity.

range fluctuation patterns in RSAs, as in Fig. 10(b), and, therefore, coherent pinning patterns due to atomic-scale distortions [43,44].

We repeated the above analysis by probing velocity fluctuations $v_x(z)$ associated with the gliding dislocations (at $\sigma > \sigma_c$) in annealed as well as random alloys (see Fig. 11). Figure 12 illustrates the shear stress dependence of the mean dislocation velocity as well as (mean) velocity correlations (averaged over different configurations) for the aged and random alloys. As shown in Fig. 12(a), the observed behavior of $\langle v_x \rangle$ versus σ at σ_c marks the dislocation pinning-to-depinning transition which is in agreement with the expected generic dependence around the transition. This seems to be fairly insensitive to annealing except for a meaningful shift of σ_c to larger strengths. The estimated critical shear stresses are $\sigma_c \simeq 950$ and 650 MPa associated with aged and random samples, respectively. The (mean) velocity autocorrelations,
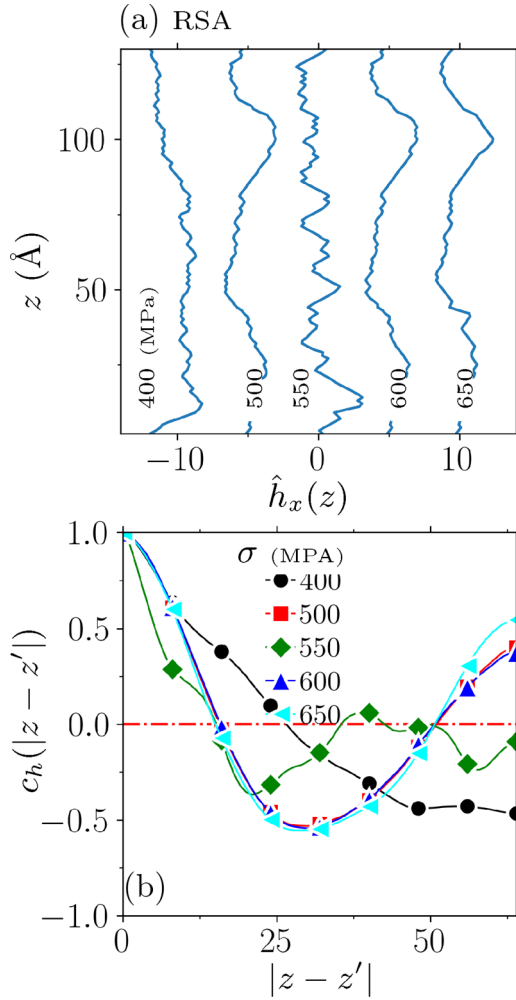
(a) RSA

FIG. 10. (a) Configurations of (immobile) partial edge dislocations and (b) associated correlations $c_h(|z - z'|) = \langle \hat{h}_x(z).\hat{h}_x(z') \rangle$ as a function of distance $|z - z'|$ in a NiCoCr RSA under different applied stresses below the depinning transition. This includes $\sigma = 400$, 500, 550, 600, and 650 MPa.

averaged over different realizations, $\langle c_v(|z - z'|) \rangle_{\text{ens}}$ [see the definition of $c_v(|z - z'|)$ below] are shown at different stress levels beyond σ_c in Figs. 12(b) and 12(c), both indicating a finite correlation length.

The marked increase of σ_c is despite (relatively) insignificant variations of elastic properties (Fig. S10) and, therefore, improving yielding properties against RSAs cannot be naively attributed to the enhancement in elasticity of aged alloys (see Sec. IV). The elastic constants we probed in this study include C_{11}, C_{12}, and C_{44} (based on the Voigt notation) as well as the bulk modulus B and Poisson's ratio that were determined by using the Li-Sheng-Ma interatomic potential. Here the x, y, and z dimensions are parallel to [100], [010], and [001] crystal directions, respectively. The overall trend we observe in Fig. S10 is consistent with the study of Li *et al.* [14] which reported the change of elastic properties with increasing SROs (on decreasing T_a). The elastic constants seem to develop features near $T_a \simeq 800$ where the dominant presence of chemical ordering is expected.

We further investigate individual dislocation configurations and associated fluctuations of local velocities in Fig. 13 and 14 where the dislocations move at an average speed $\langle v_x \rangle \simeq 1000 \text{ ms}^{-1}$ in both systems subject to the applied shear stress of $\sigma = 1200$ MPa, well above the corresponding depinning thresholds. The (z-scored) velocity profiles $\hat{v}_x(z)$ in Figs. 13(a) and 14(a) correspond to five different snapshots of gliding dislocations that are shifted for a better view of variations across the (average) dislocation line direction z. We remark that the regions to the left of the dash-dotted lines indicate local velocities below the average speed $\langle v_x \rangle$, as depicted by the left-headed arrows in Fig. 11 . Statistically speaking, the segments with $v_x(z) < \langle v_x \rangle$ somewhat correlate with the positively bent segments of dislocation lines which are mostly influenced by the existence of SROs and/or atomic misfits. Nevertheless, velocity fluctuations quantified by the velocity auto correlations,

$$c_v(|z - z'|) = \langle \hat{v}_x(z).\hat{v}_x(z') \rangle, \tag{3}$$

does not appear to be statistically different in annealed and random alloys in Figs. 13(b) and 14(b).

IV. DISCUSSIONS AND CONCLUSIONS

Our atomistic simulations of NiCoCr CSAs under special thermal treatments have revealed the formation of nanostructural local chemical ordering and enhanced dislocation glide resistance in close agreement with recent SRO-based studies in simulated and *real* NiCoCr experiments [5,14]. On the ordering effects, we made use of the Li-Sheng-Ma potential function that has been validated in terms of detailed and accurate modeling of Ni, Co, and Cr interatomic interactions [14]. Our direct measurements of local lattice strains agree very closely with a recent *ab initio* study [37] but failed to fully reproduce experimental findings [9]. By using the Farkas-Caro potential, we find very limited relevance to real annealed NiCoCr alloys. The simulated alloys, in this context, exhibit no ordering (beyond statistical fluctuations) but also no notable improvement in yield strengths or elastic properties as reported in Table I in the Supplemental Material (see also Refs. [4,45]). We have interpreted the physical origin of such differences by using robust (experimentally relevant) SRO descriptors in various thermal annealing scenarios. We find that the Li-Sheng-Ma potential, under the proper aging process, leads to an exceptional dislocation depinning strength with low stacking fault width that falls short of that of RSAs. The latter is associated with the enhanced stacking fault energy which might, in part, relate to improved elasticity as a result of SROs but, compared to the yield strength, the ordering effects appear to be less pronounced. The intrinsic strengthening mechanism is mostly dominated by coherent SROs-induced pinning effects, but random spatial distributions of misfit volumes and the resulting roughening seem to be also at play.

Our correlation analyses of the dislocation structure and its spatial-temporal evolution allow for inferring a characteristic pinning length ξ_p and optimal displacement w_p [25]. We interpret the latter as being the rms fluctuations in the dislocation height (with respect to the mean), i.e., $w_p = \langle h_x^2 - \langle h_x \rangle^2 \rangle^{\frac{1}{2}}$, whereas the former is determined as the shortest distance
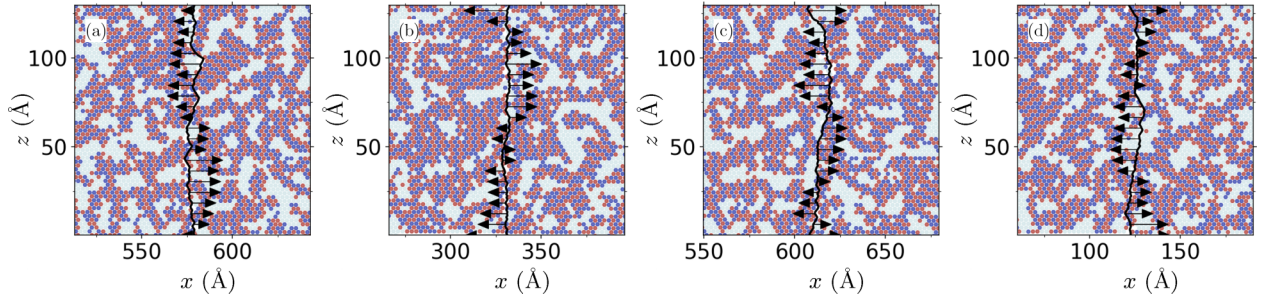
FIG. 11. (z-Scored) Velocity of partial edge dislocations $\hat{v}_x(z)$, illustrated by the black arrows, in annealed NiCoCr at $T_a = 600\,\mathrm{K}$ and under the applied stress $\sigma = 1200\,\mathrm{MPa}$ (above σ_c). The shear tests were carried out at 5 K. Here the panels indicate different realizations associated with the gliding dislocations and the two-dimensional plane denotes a (111) cross section. The arrows denote the velocity field.

where the height correlations cross zero, e.g., $c_h(|z - z'|) = 0$ at $|z - z'| = \xi_p$. At $T_a = 600\,\mathrm{K}$ and $\sigma < \sigma_y$, it follows that $w_p = 5.6–11.2\,\text{Å}$ and $\xi_p = 25–31\,\text{Å}$ associated with the annealed alloy. We conjecture that these two quantities should both correlate with the observed increase in the depinning stress. Based on our present data, however, we are not able to quantify such (anti-)correlations numerically. Both observables w_p and ξ_p are also expected to show meaningful associations with the average SRO size ξ^{sro} as well as the amplitude of misfit fluctuations (characterized by ξ^{misfit}) and are relevant ingredients in *mean-field* solute models that make yield strength predictions based on dislocation line properties (e.g., line tension Γ, length L, and Burgers vector b). In this mean-field picture, SROs introduce the characteristic scale ξ^{sro} that *effectively* decreases the pinning length ξ_p leading to a reduction of the optimal displacement w_p and, therefore, an extra strengthening. Within these mean-field model frameworks, the depinning stress should scale with the line tension Γ, which itself is proportional to the shear modulus and, based on our findings, annealing is not expected to boost σ_y simply because of such elasticity-based contributions but instead variations in the disorder strength and the pinning field are the key factors. To validate such theories in simulations, one must be vigilant to use appropriate mesoscopic lengths (beyond atomistic scales) where continuum-like concepts such as line tension and local curvature are well defined [25]. To explore the full dislocation waviness in MD, it is also necessary that the dislocation length $L \gg \xi_p$ and associated

deformation $w_p \ll \xi_p$ [46]. However, the above separation of scales is typically a limit beyond atomistic modeling assumptions including the present study.

Complications might also arise in the application of strengthening theories (e.g., the VC model) due to SRO-induced correlations. The latter are at odds with the "randomness" hypothesis taken as granted based on solutes' arrangements in RSAs. Given that the VC theory is constructed exclusively on misfit information, an *effective* treatment in the presence of spatial correlations is the assumption that SROs should alter dramatically local misfit distributions and, in that case, an alternative length $\xi^{\mathrm{misfit}}_{\mathrm{eff}}$ may be used to describe the strength of distortions. Alternatively, Zaiser and Wu (ZW) [44,47] formulated a more relevant approach based on the fact that pinning forces caused by obstacles are not fully random but rather correlated over some certain length a [48] that we tend to interpret as the effective SRO size ($a \simeq \xi^{\mathrm{sro}}$). In their formulation of dislocation dynamics, ZW introduced a order/disorder length that, along with the strength of misfit fluctuations, may describe the SRO- and misfit-induced noise field in a more accurate way than the VC methodology. Similar efforts were made by Zhang *et al.* [49] along these lines who developed a stochastic Peierls-Nabarro model to incorporate the role of both CSA randomness and short-range ordering effects on glide dynamics of roughened dislocations.

The existing literature reports the emergence of (varying degrees of) SROs as a rather generic feature across a broad
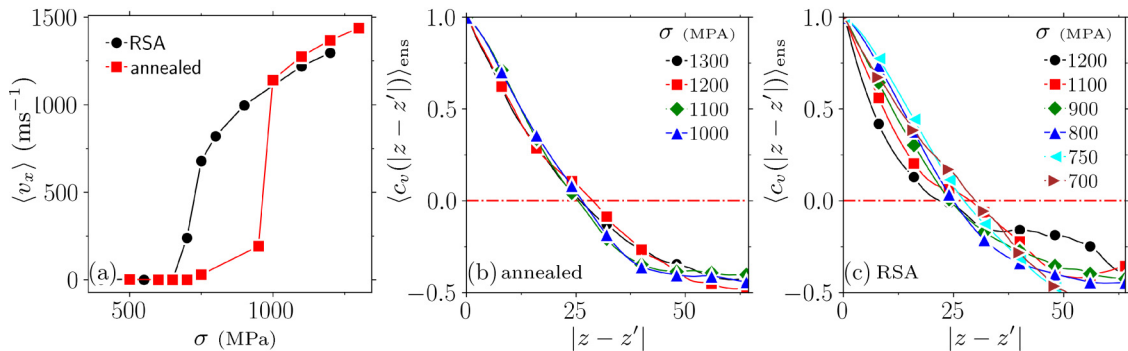

FIG. 12. Stress dependence of the mean dislocation velocity and associated fluctuations. (a) Mobility rule describing the mean dislocation velocity $\langle v_x \rangle$ as a function of applied stress σ. Mean velocity auto correlations $\langle c_v(|z - z'|)\rangle_{\mathrm{ens}}$ as a function of distance $|z - z'|$ in (b) annealed NiCoCr and (c) NiCoCr RSA subject to multiple applied stresses σ above σ_y.
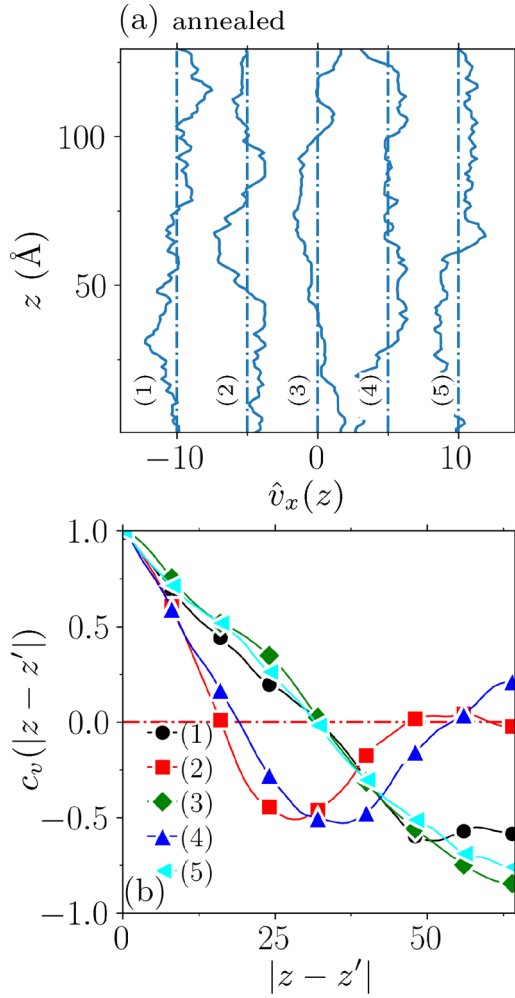
FIG. 13. (a) (Scaled) velocity of partial edge dislocations $\hat{v}_x(z)$ and (b) associated correlations $c_v(|z - z'|) = \langle \hat{v}_x(z).\hat{v}_x(z') \rangle$ as a function of distance $|z - z'|$ in an annealed NiCoCr at $T_a = 600\,\mathrm{K}$ under the applied stress $\sigma = 1200$ MPa (above σ_c). The shear tests were carried out at 5 K. Here the numbers indicate different realizations associated with gliding dislocations and the two-dimensional plane denotes a (111) cross section. The velocity profiles are shifted vertically for the clarity.

FIG. 14. (a) (Scaled) velocity of partial edge dislocations $\hat{v}_x(z)$ and (b) associated correlations $c_v(|z - z'|) = \langle \hat{v}_x(z).\hat{v}_x(z') \rangle$ as a function of distance $|z - z'|$ in a NiCoCr RSA under the applied stress $\sigma = 1200$ MPa (above σ_c).

range of high-entropy alloys (see Ref. [6] and references therein). Nevertheless, the focus has been placed on different variants of NiCoCr-based alloys (including the well-studied Cantor alloy) and, owing to similar atomic size and electron negativity, such compositions might tend to favor SRO nucleation [50]. In terms of mechanical properties, the SRO-induced enhancement in the dislocation glide resistance may also constitute fairly universal mechanisms associated with it, i.e., coherent pinning and enhanced roughening, not specific to particular chemical compositions but their robustness over a broader range of compositionally complex solid solutions has yet to be fully explored.

There is a large multitude of results in this work, some of which including the dislocation roughening and SRO emergence could be potentially validated experimentally through the *in/ex situ* electron microscopy analysis or other image-base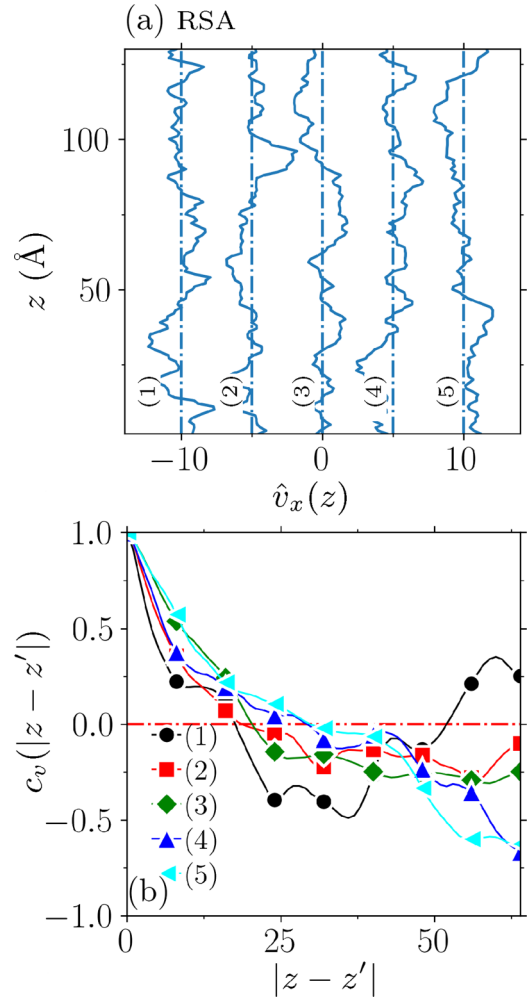d characterization techniques. Similar efforts were made by Sandfeld *et al.* [43] based on the image processing of *in situ* electron microscopy micrographs to obtain dislocation velocity profiles in a deforming NiCoCrFeMn (Cantor) alloy. Based on their observations, kinematics of dislocation lines and associated pinning patterns suggest the direct relevance of lattice distortions as the dominant roughening mechanism. On the other hand, SROs and associated pinning effects are more subtle to be detected experimentally owing to their nanoscopic origins.

Our finding will have important implications for discrete dislocation dynamics (DDD) models and associated mobility rules that additionally consider spatial correlations within the rough potential energy landscape [51]. This is conceptually similar to intrinsic Peierls stresses that are locally distributed in space but also correlated over certain microstructural scales. Incorporating and tuning SROs' structural features as model ingredients will potentially lead to further improvements in DDD predictive capabilities and design-level hardening features in the context of NiCoCr-based CSAs with dense and complex networks of interacting dislocations.

[1] Z. Li, S. Zhao, R. O. Ritchie, and M. A. Meyers, Mechanical properties of high-entropy alloys with emphasis on face-centered cubic alloys, Prog. Mater. Sci. **102**, 296 (2019).

[2] Y. Shang, J. Brechtl, C. Psitidda, and P. K. Liaw, *Mechanical Behavior of High-Entropy Alloys: A Review, High-Entropy Materials Theory, Experiments, and Applications* (Springer, Cham, 2021), pp. 435–522.

[3] Containing equal numbers of Ni, Co, and Cr atoms.

[4] B. Gludovatz, A. Hohenwarter, K. V. S. Thurston, H. Bei, Z. Wu, E. P. George, and R. O. Ritchie, Exceptional damage-tolerance of a medium-entropy alloy CrCoNi at cryogenic temperatures, Nat. Commun. **7**, 10602 (2016).

[5] R. Zhang, S. Zhao, J. Ding, Y. Chong, T. Jia, C. Ophus, M. Asta, R. O. Ritchie, and A. M. Minor, Short-range order and its impact on the CrCoNi medium-entropy alloy, Nature (London) **581**, 283 (2020).

[6] Y. Wu, F. Zhang, X. Yuan, H. Huang, X. Wen, Y. Wang, M. Zhang, H. Wu, X. Liu, H. Wang *et al.*, Short-range ordering and its effects on mechanical properties of high-entropy alloys, J. Mater. Sci. Technol. **62**, 214 (2021).

[7] L. Zhou, Q. Wang, J. Wang, X. Chen, P. Jiang, H. Zhou, F. Yuan, X. Wu, Z. Cheng, and E. Ma, Atomic-scale evidence of chemical short-range order in CrCoNi medium-entropy alloy, Acta Mater. **224**, 117490 (2022).

[8] X. Chen, Q. Wang, Z. Cheng, M. Zhu, H. Zhou, P. Jiang, L. Zhou, Q. Xue, F. Yuan, J. Zhu *et al.*, Direct observation of chemical short-range order in a medium-entropy alloy, Nature (London) **592**, 712 (2021).

[9] B. Yin, S. Yoshida, N. Tsuji, and W. Curtin, Yield strength and misfit volumes of NiCoCr and implications for short-range-order, Nat. Commun. **11**, 1 (2020).

[10] W. G. Noehring and W. Curtin, Correlation of microdistortions with misfit volumes in high entropy alloys, Scr. Mater. **168**, 119 (2019).

[11] L. Liu, Y. Zhang, J. Han, X. Wang, W. Jiang, C.-T. Liu, Z. Zhang, and P. K. Liaw, Nanoprecipitate-strengthened high-entropy alloys, Adv. Sci. **8**, 2100870 (2021).

[12] Q. He, P. Tang, H. Chen, S. Lan, J. Wang, J. Luan, M. Du, Y. Liu, C. Liu, C. Pao *et al.*, Understanding chemical short-range ordering/demixing coupled with lattice distortion in solid solution high entropy alloys, Acta Mater. **216**, 117140 (2021).

[13] C. Wolverton, V. Ozolins, and A. Zunger, Short-range-order types in binary alloys: A reflection of coherent phase stability, J. Phys.: Condens. Matter **12**, 2749 (2000).

[14] Q.-J. Li, H. Sheng, and E. Ma, Strengthening in multi-principal element alloys with local-chemical-order roughened dislocation pathways, Nat. Commun. **10**, 3563 (2019).

[15] F. Walsh, M. Asta, and R. O. Ritchie, Magnetically driven short-range order can explain anomalous measurements in crconi, Proc. Natl. Acad. Sci. USA **118**, e2020540118 (2021).

[16] F. Zhang, S. Zhao, K. Jin, H. Xue, G. Velisa, H. Bei, R. Huang, J. Ko, D. Pagan, J. Neuefeind *et al.*, Local Structure and Short-Range Order in a NiCoCr Solid Solution Alloy, Phys. Rev. Lett. **118**, 205501 (2017).

[17] J. Wang, P. Jiang, F. Yuan, and X. Wu, Chemical medium-range order in a medium-entropy alloy, Nat. Commun. **13**, 1021 (2022).

[18] J. Ding, Q. Yu, M. Asta, and R. O. Ritchie, Tunable stacking fault energies by tailoring local chemical order in CrCoNi medium-entropy alloys, Proc. Natl. Acad. Sci. USA **115**, 8919 (2018).

[19] X. Yang, Y. Xi, C. He, H. Chen, X. Zhang, and S. Tu, Chemical short-range order strengthening mechanism in CoCrNi medium-entropy alloy under nanoindentation, Scr. Mater. **209**, 114364 (2022).

[20] W.-R. Jian, Z. Xie, S. Xu, Y. Su, X. Yao, and I. J. Beyerlein, Effects of lattice distortion and chemical short-range order on the mechanisms of deformation in medium entropy alloy CoCrNi, Acta Mater. **199**, 352 (2020).

[21] D. Liu, Q. Yu, S. Kabra, M. Jiang, P. Forna-Kreutzer, R. Zhang, M. Payne, F. Walsh, B. Gludovatz, M. Asta *et al.*, Exceptional fracture toughness of crconi-based medium-and high-entropy alloys close to liquid helium temperatures, Science **378**, 978 (2022).

[22] J. Miao, C. Slone, S. Dasari, M. Ghazisaeidi, R. Banerjee, E. P. George, and M. J. Mills, Ordering effects on deformation substructures and strain hardening behavior of a crconi based medium entropy alloy, Acta Mater. **210**, 116829 (2021).

[23] S. S. Sohn, A. Kwiatkowski da Silva, Y. Ikeda, F. Körmann, W. Lu, W. S. Choi, B. Gault, D. Ponge, J. Neugebauer, and D. Raabe, Ultrastrong medium-entropy single-phase alloys designed via severe lattice distortion, Adv. Mater. **31**, 1807142 (2019).

[24] R. Labusch, A statistical theory of solid solution hardening, Phys. Status Solidi B **41**, 659 (1970).

[25] C. Varvenne, A. Luque, and W. A. Curtin, Theory of strengthening in fcc high entropy alloys, Acta Mater. **118**, 164 (2016).

[26] C. Varvenne, G. P. M. Leyson, M. Ghazisaeidi, and W. A. Curtin, Solute strengthening in random alloys, Acta Mater. **124**, 660 (2017).

[27] C. Varvenne and W. A. Curtin, Predicting yield strengths of noble metal high entropy alloys, Scr. Mater. **142**, 92 (2018).

[28] D. Utt, S. Lee, Y. Xing, H. Jeong, A. Stukowski, S. H. Oh, G. Dehm, and K. Albe, The origin of jerky dislocation motion in high-entropy alloys, Nat. Commun. **13**, 4777 (2022).

[29] A. P. Thompson, H. M. Aktulga, R. Berger, D. S. Bolintineanu, W. M. Brown, P. S. Crozier, P. J. in 't Veld, A. Kohlmeyer, S. G. Moore, T. D. Nguyen, R. Shan, M. J. Stevens, J. Tranchida, C. Trott, and S. J. Plimpton, LAMMPS—A flexible simulation tool for particle-based materials modeling at the atomic, meso, and continuum scales, Comput. Phys. Commun. **271**, 108171 (2022).

[30] F.-H. Cao, Y.-J. Wang, and L.-H. Dai, Novel atomic-scale mechanism of incipient plasticity in a chemically complex crconi

medium-entropy alloy associated with inhomogeneity in local chemical environment, Acta Mater. **194**, 283 (2020).

[31] D. Farkas and A. Caro, Model interatomic potentials and lattice strain in a high-entropy alloy, J. Mater. Res. **33**, 3218 (2018).

[32] B. Sadigh, P. Erhart, A. Stukowski, A. Caro, E. Martinez, and L. Zepeda-Ruiz, Scalable parallel Monte Carlo algorithm for atomistic simulations of precipitation in alloys, Phys. Rev. B **85**, 184203 (2012).

[33] See Supplemental Material at http://link.aps.org/supplemental/10.1103/PhysRevB.107.094109 for further discussions relevant to simulation details, characterization of local ordering, and yield properties corresponding to model NiCoCr alloys.

[34] C. A. Becker, M. Asta, J. J. Hoyt, and S. M. Foiles, Equilibrium adsorption at crystal-melt interfaces in lennard-jones alloys, J. Chem. Phys. **124**, 164708 (2006).

[35] Y. N. Osetsky and D. J. Bacon, An atomic-level model for studying the dynamics of edge dislocations in metals, Modell. Simul. Mater. Sci. Eng. **11**, 427 (2003).

[36] We only report the (excess) configurational heat capacity (and thermal expansion coefficient) neglecting (ideal) kinetic contributions.

[37] H. S. Oh, S. J. Kim, K. Odbadrakh, W. H. Ryu, K. N. Yoon, S. Mu, F. Körmann, Y. Ikeda, C. C. Tasan, D. Raabe *et al.*, Engineering atomic-level complexity in high-entropy and complex concentrated alloys, Nat. Commun. **10**, 1 (2019).

[38] D. Hull and D. J. Bacon, *Introduction to Dislocations* (Butterworth-Heinemann, Oxford, 2001).

[39] Y. N. Osetsky, G. M. Pharr, and J. R. Morris, Two modes of screw dislocation glide in fcc single-phase concentrated alloys, Acta Mater. **164**, 741 (2019).

[40] M. Zaiser, Scale invariance in plastic flow of crystalline solids, Adv. Phys. **55**, 185 (2006).

[41] A. Esfandiarpour, S. Papanikolaou, and M. Alava, Edge dislocations in multicomponent solid solution alloys: Beyond

traditional elastic depinning, Phys. Rev. Res. **4**, L022043 (2022).

[42] A. Stukowski, V. V. Bulatov, and A. Arsenlis, Automated identification and indexing of dislocations in crystal interfaces, Modell. Simul. Mater. Sci. Eng. **20**, 085007 (2012).

[43] C. Zhang, H. Song, D. Oliveros, A. Fraczkiewicz, M. Legros, and S. Sandfeld, Data-mining of in-situ tem experiments: On the dynamics of dislocations in CoCrFeMnNi alloys, Acta Mater. **241**, 118394 (2022).

[44] M. Zaiser and R. Wu, Pinning of dislocations in disordered alloys: Effects of dislocation orientation, arXiv:2109.07796.

[45] G. Laplanche, M. Schneider, F. Scholz, J. Frenzel, G. Eggeler, and J. Schreuer, Processing of a single-crystalline crconi medium-entropy alloy and evolution of its thermal expansion and elastic stiffness coefficients with temperature, Scr. Mater. **177**, 44 (2020).

[46] W. A. Curtin (private communication, 2022).

[47] A. Vaid, D. Wei, E. Bitzek, S. Nasiri, and M. Zaiser, Pinning of extended dislocations in atomically disordered crystals, arXiv:2110.12507.

[48] P.-A. Geslin, A. Rida, and D. Rodney, Microelasticity model of random alloys. part ii: Displacement and stress correlations, J. Mech. Phys. Solids **153**, 104480 (2021).

[49] L. Zhang, Y. Xiang, J. Han, and D. J. Srolovitz, The effect of randomness on the strength of high-entropy alloys, Acta Mater. **166**, 424 (2019).

[50] Q. Ding, Y. Zhang, X. Chen, X. Fu, D. Chen, S. Chen, L. Gu, F. Wei, H. Bei, Y. Gao *et al.*, Tuning element distribution, structure and properties by composition in high-entropy alloys, Nature (London) **574**, 223 (2019).

[51] H. Salmenjoki, A. Lehtinen, L. Laurson, and M. J. Alava, Plastic yielding and deformation bursts in the presence of disorder from coherent precipitates, Phys. Rev. Mater. **4**, 083602 (2020).